scientific reports

OPEN

Insights from indoor testing and numerical simulations of the Lanniqing Landslide in Zhaotong, Yunnan Province, China

Xu Zongheng[1,2]✉ & **Chen Yunying**[1,2]

Rainfall-induced landslides are a prevalent phenomenon in the mountainous regions of southwestern China, attracting significant research interest regarding their processes and mechanisms. Field investigations and laboratory tests yield crucial data on the physical and mechanical properties of the landslide material and the deformation of slope movement. Furthermore, numerical simulations create a feedback mechanism with field and lab findings, enhancing our comprehensive understanding of the occurrence processes and mechanisms underlying rainfall-induced landslides. This paper focuses on the Lanniqing landslide, located in Zhaotong City, Yunnan Province, Southwest China. It employs field investigations and laboratory tests to examine the physical, shear, and compression mechanical properties of the sliding-zone soil. Additionally, numerical models are developed to analyze the deformation characteristics and slope stability conditions under various conditions. The results indicate that the soils from the sliding zone of the landslide have high fine grain content, primarily consisting of low liquid limit clay. These soils exhibit high cohesion and low friction angle, classifying them as medium–high compressibility based on the compression test results. Additionally, their poor shear and compression mechanical properties serve as a critical factor contributing to the occurrence of landslides. Under natural and rainfall conditions, the slope generally remains stable; however, slope cutting has a significant impact on stability, leading to an unstable state. The coupling of multiple factors leads to a substantial increase in shear strain and slope deformation. Furthermore, the continuous load from the Shan-ma road at the trailing edge exacerbates the slope's instability. These findings are crucial for understanding the formation of similar rainfall-induced landslides in Southwest China and offer valuable insights for the prevention and management of slope disasters influenced by various factors.

Keywords Rainfall-induced landslide, In-situ tests, Stability analysis, Finite element modelling, Landslide occurrence

China is one of the countries most affected by geological disasters in the world, with rainfall-induced landslides being particularly common. These landslides exhibit significant regional characteristics, especially in the southwestern region, where the abundance of mountainous terrain and concentrated rainfall lead to severe landslide disasters. Yunnan Province is one of the regions most affected by rainfall-induced landslide disasters, characterized by its extensive distribution, significant scale, high frequency, and severe impacts, making it remarkable both nationally and globally. In-depth research on slope stability analysis, evaluation methods, and failure mechanisms in the mountainous watersheds of Yunnan is crucial for foundational understanding and holds significant academic value, as well as important theoretical significance and practical implications.

In the study of rainfall-induced landslides, methods such as field observations, laboratory tests, and physical modeling facilitate the assessment of the physical, mechanical characteristics and hydrological processes[1] of the landslide mass under varying conditions. These methods also enable the monitoring of slope displacement, deformation, and failure, providing essential foundational data for the research. Numerical simulations primarily employ finite element methods, which are crucial for stability analysis[2]. These simulations can model displacement fields, stress fields, seepage fields, and coupled models during rainfall events[3], thereby enhancing

[1]Faculty of Geography, Yunnan Normal University, Kunming 650500, China. [2]Key Laboratory of Plateau Geographic Processes and Environment Change of Yunnan Province, Kunming 650500, Yunnan, China. ✉email: 140079@ynnu.edu.cn

our understanding of the mechanisms underlying rainfall-induced landslides. Additionally, evaluating slope stability and investigating failure mechanisms through numerical simulations are important research areas, with the FLAC (Fast Lagrangian Analysis of Continua) method offering substantial convenience for these studies[4]. This method is capable of simulating three-dimensional structures made from soil, rock, or other materials, offering up to 10 material models to more accurately replicate the mechanical properties of real-world materials[5]. It has been extensively applied and further developed in various fields, including slope stability analysis, pile foundation remediation[6,7], ancient landslide stability assessments[8,9], mining slope excavation and deformation[10,11], as well as deformation in landfills and embankments[12].

FLAC3D is renowned for its high computational efficiency, minimal data storage requirements, and the use of a more precise and rational hybrid discrete method to simulate the plastic failure and flow characteristics of materials. It offers significant advantages over traditional finite element methods[13–16]. In addition to simulating material behavior in three dimensions, FLAC3D provides deeper insights into the failure mechanisms of geological phenomena, making it a valuable tool for engineering practice.FLAC3D can also be integrated with other software or computational methods to enhance slope stability analysis and failure mechanism research. For instance, Ahmed et al.[17] explored the effectiveness of this approach by analyzing the impact of shear strength and geometric parameters on the safety factor using Geo5, FLAC3D, and ABAQUS. Li et al.[18] utilized the updated Mathews graph method to evaluate stability probabilities and employed FLAC3D simulations to assess maximum displacement, plastic zone volume, and maximum principal stress. FLAC3D allows for convenient secondary development, enabling users to tailor the software to their specific research needs. For instance, Wang et al.[19] developed a strength reduction method that accounts for rheological properties through FLAC3D secondary development. Xu et al.[20] utilized seepage field data and custom FLAC3D modifications to simulate the landslide evolution process in the stability analysis. FLAC3D has significantly contributed to the study of slope stability by allowing researchers to simulate its evolution under various geological conditions and environmental factors. Key influencing factors, such as shear strength parameters[17], stratigraphic structure[9,21], excavation patterns[2,7,22], and external forces like reservoir impoundment[23,24], rainfall[25,26] and seismic activity[9,27], have been shown to play critical roles in slope stability. With its high-precision simulation capabilities, FLAC3D serves as a powerful and indispensable tool in advancing slope stability research.

Numerical simulations of rainfall-induced landslides are often integrated with both indoor and outdoor experimental results, a crucial step in enhancing model accuracy and reliability. Laboratory tests, such as strength and permeability assessments, provide essential parameters for setting up the numerical model, while field monitoring data on landslide deformation are critical for validating its accuracy. This integration of numerical simulations with experimental data forms a feedback loop, allowing for a more comprehensive understanding of rainfall-induced landslide processes. In this study, we investigate the Lanniqing landslide in Zhaotong, Yunnan Province, China. Unlike traditional single-factor or simplistic multi-factor approaches, this research systematically establishes the slope stability analysis framework integrating "physical–mechanical experiments—excavation simulation—rainfall coupling simulation—comprehensive coupling analysis." By incorporating field investigations and laboratory test results into FLAC3D simulations, we analyze the slope response to excavation, rainfall, and their interactions, grounded in the comprehensive understanding of the physical–mechanical properties of the sliding-zone soil. This approach ultimately uncovers the underlying causes triggering the Lanniqing landslide.

Materials and methods

Study site and sampling

The Lanniqing landslide study area is located in Xiaohe Town, Qiaojia County, Zhaotong City, Yunnan Province, China. Qiaojia County shares borders with Dongchuan County in Kunming, Huize County in Qujing, and Ludian and Zhaoyang Counties in Zhaotong. It is separated from Huidong County in Sichuan Province's Liangshan Prefecture by the Jinsha River (Fig. 1a,b). Geologically, Qiaojia sits within the Sichuan-Yunnan meridian structural system, at the junction of the northern Sichuan-Yunnan meridian structural belt's eastern margin and the eastern Yunnan structural region. The Yaoshan tectonic belt is the area's primary structural feature, with geological activity largely shaped by fault movements[28]. This region is characterized by significant geological instability due to fault zones and tectonic erosion in its high mountain gorge landscape, particularly along the Niulan River. As a result, it is prone to frequent geological disasters that have caused substantial economic damage and loss of life.In-situ testing samples for this study were collected from Lanniqing Village in Xiaohe Town, where the landslide occurred on the northeastern slope of the village at approximately 4:40 a.m. on September 5, 2019, following a period of prolonged heavy rainfall. Around 100,000 cubic meters of fragmented mudstone, mixed with gray and purple clay as well as sub-clay, rapidly slid down the slope. The significant elevation difference exacerbated the disaster, leading to the landslide that buried two households, resulted in nine fatalities, and caused extensive property damage, culminating in severe human and economic losses (Fig. 1c).

The terrain in the Lanniqing landslide area features the steep incline from west to east, with pronounced elevation variations. Field investigations identified three distinct sections of the Lanniqing landslide: the source area, the flow area, and the deposition-disaster-causing area (Fig. 2a). The source area primarily consists of the area enclosed by the Shan-ma Road, the Lanniqing village path, and the adjacent sidewalls. The sliding surface has a slope of approximately 42°, extending about 300 m longitudinally and 44–50 m in width. The landslide spans an area of roughly 14,000 square meters, with a thickness of 5–10 m, and an estimated volume of 100,000 cubic meters, classifying it as small-scale landslide[29]. The landslide's trailing edge is marked by a distinct scarp, with the Shan-ma Road located directly above it. Due to the impact of the landslide, parts of the road surface have become unsupported, posing a risk of further damage (Fig. 2b).The middle section of the slope, spanning approximately 180 m, constitutes the landslide's movement zone. This area is characterized by the presence

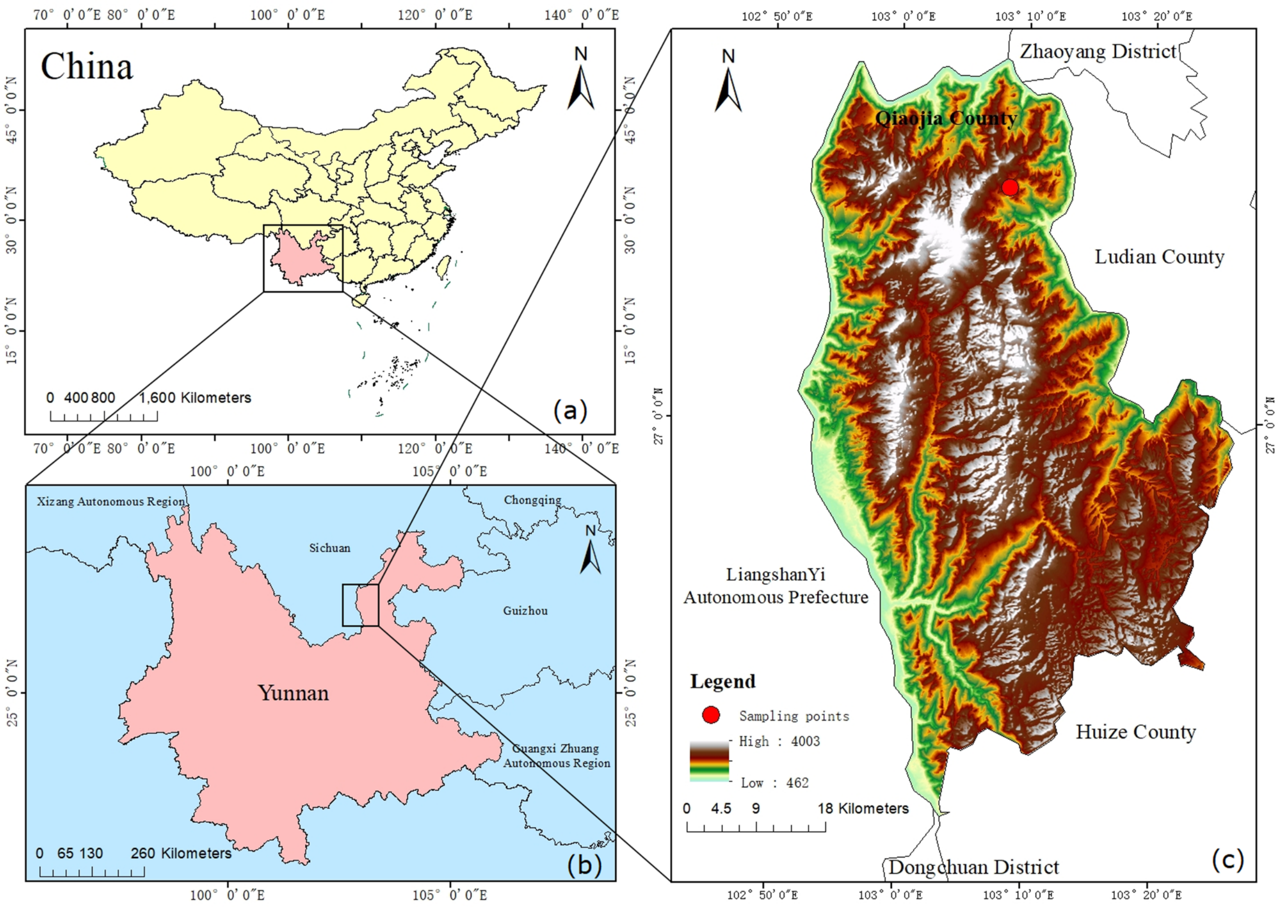

Fig. 1. Geographical location map of the study area. The map was created using ArcGIS 10.8 (https://desktop.arcgis.com/zh-cn/desktop/index.html). Data sources:Digital Elevation Model (DEM): https://www.gscloud.cn/ Vector boundaries: Review number GS Jing (2022) 1061, data available at http://datav.aliyun.com/portal/school/atlas/area_selector. Basemap: https://www.geosceneonline.cn/geoscene/webapps/home.

of mudstone blocks of varying sizes in the upper portion. Observations reveal that the stability of these rock and soil masses is relatively weak. The mudstone shows pronounced softening upon contact with water and crumbles when dried, conditions that greatly contributed to the initiation of the Lanniqing landslide (Fig. 2c,d). Additionally, fallen trees were observed on both sides of this area, indicating a noticeable air wave effect during the downslope movement of the landslide mass (Fig. 2e). The disaster zone was primarily concentrated in Lanniqing Village, where the landslide, after moving along its path, surged over the steep slope behind the village. It destroyed and buried houses, eventually settling at the base of an approximately 15-m-high scarp (Fig. 2f). The on-site rescue efforts revealed that the landslide mass had a high water content and significant viscosity, which posed considerable challenges for the rescue operations(Fig. 2f). According to meteorological data, from 8:00 p.m. on September 4 to 8:00 a.m. on September 5, 2019, the Lanniqing area experienced 190.7 mm of rainfall over a 12-h period, classifying it as an extreme rainstorm[30]. Consequently, the Lanniqing landslide was identified as rainfall-induced landslide[29]. To thoroughly understand the physical and mechanical properties of the landslide soil, samples were taken from two locations in the sliding source area, designated as QJ1 and QJ2 (Fig. 2a). Sampling sites were chosen in areas with minimal human disturbance, where surface piles and debris caused by rainfall runoff were cleared. Soil samples for testing were collected from a smooth surface at 20-cm intervals down to a depth of one meter, and were sequentially labeled QJ1-1 to QJ1-5 and QJ2-1 to QJ2-5 (Fig. 3a).

In-situ testing method

Physical experiments

The physical experiments involved particle size analysis and Atterberg limit testing. Prior to particle size analysis, the soil samples underwent pre-treatment. Each 0.2-g sample was treated with 10 mL of 10% H_2O_2 and heated on hot plate until bubbling ceased. The hot plate temperature was typically set at 85 °C to promote the reaction while avoiding excessive intensity. The solution was then removed, and 10 mL of 0.05 mol/L $(NaPO_3)_6$ was added, with the mixture being agitated in an ultrasonic cleaner for 10 min at a frequency of 40 kHz. Particle size analysis was conducted using Mastersizer 2000 (Fig. 3d), which measures particles in the range of 0.02–2000 μm. The samples were air-dried and sieved through 2 mm mesh. To ensure accuracy, each sample was tested three

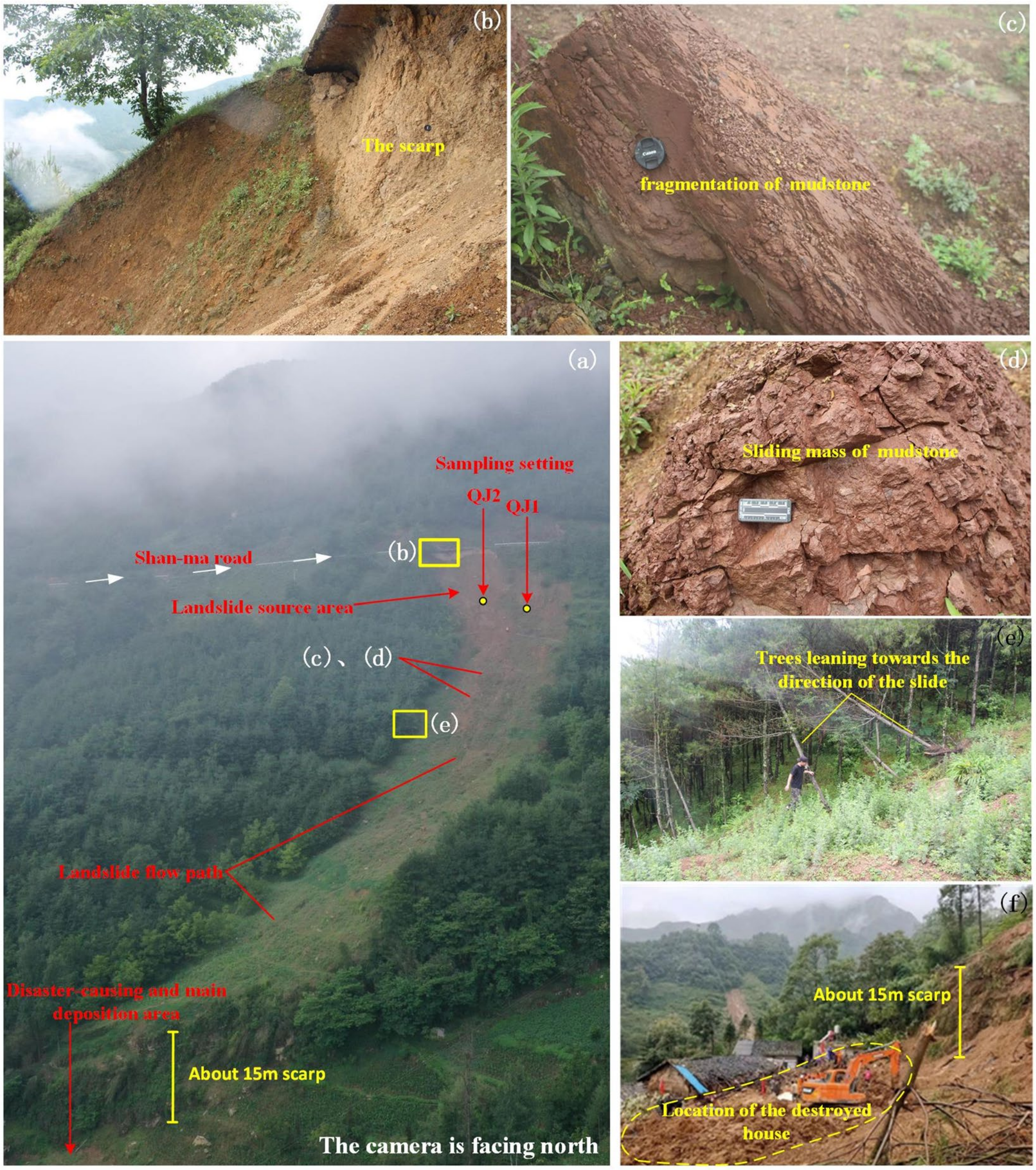

Fig. 2. General view and site survey of Lanniqing landslide. (**a**) Panoramic view of the landslide. (**b**) ~ (**e**) Photographs of the rear scarp and the sliding zone of the landslide captured by research team during the field investigation. (**f**) The scene rescue image from Zhaotong Daily (China).

times, and the average result was used for analysis. The Atterberg limits were determined using a liquid-plastic limit tester manufactured by the Nanjing Soil Instrument Factory in China.

Mechanical property tests

The mechanical property tests consisted of direct shear and compression tests. The direct shear tests were conducted using shear apparatus manufactured by the Nanjing Soil Instrument Factory in China (Fig. 3b). Four samples were tested under vertical pressures of 100 kPa, 200 kPa, 300 kPa, and 400 kPa, and were loaded at the constant rate of 1.2 mm/min, resulting in failure within 3–5 min. Shear strength and related parameters were determined based on the classical Mohr–Coulomb failure criterion. For the compression tests, the applied load levels were 100 kPa, 100 kPa, 200 kPa, and 400 kPa, with each load maintained for 24 h (Fig. 3c). After stabilization under each load, the next level of pressure was applied. The results were used to calculate the void ratio for each load level, and the compression coefficient was determined to evaluate the soil compressibility of samples.

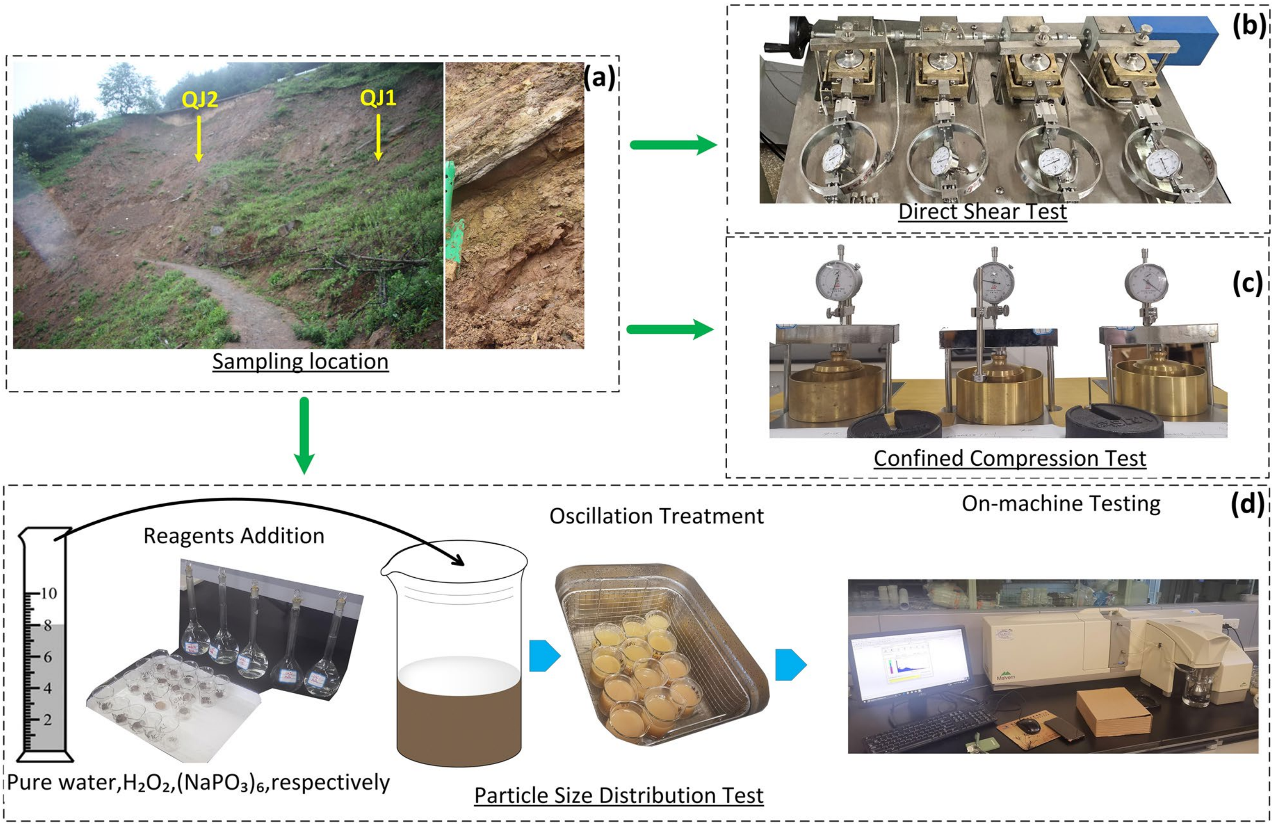

Fig. 3. Indoor testing methods for soil samples. (**a**) Sampling locations and field sampling; (**b**) Quadruple direct shear test; (**c**) Confined compression test; (**d**) Pre-treatment and instrument-based analysis of particle size.

Numerical simulation method

To gain the deeper understanding of the formation and evolution of the landslide, FLAC3D numerical simulations were employed to model the effects of external condition changes on the stability and deformation characteristics of the slope, revealing the underlying mechanisms of the landslide.

Slope model and parameters

Based on field investigations and the 1:200,000 geological map of China, the simplified two-layer slope model was established, consisting of Ordovician Middle-Upper DaQing Formation mudstone (bedrock) and the overlying residual soil (Fig. 4a), while omitting small-scale surface irregularities. This simplification was conducted to ensure the reliability of the analysis results while facilitating the simulation process, improving computational efficiency, and optimizing storage requirements. To address the limitations of FLAC3D in the preprocessing stage, particularly in generating complex meshes, researchers have refined various approaches, including integrating AutoCAD with FLAC3D, utilizing 3DEC to construct dynamic models[31], and establishing an FLAC3D-ANSYS interface[32]. In this study, the three-dimensional slope model based on cross-sections was constructed using ANSYS 2019R1 (https://www.ansys.com), followed by mesh generation. The model was then imported into FLAC3D 5.00 (Fast Lagrangian Analysis of Continua in 3 Dimensions, https://www.itascacg.com/software/flac3d) via the ANSYS-FLAC3D interface to enhance computational efficiency and accuracy in numerical simulations. The model measures 300 m in length and 170 m in height and consists of three material groups: clinosol and residual soil, mudstone, and excavated soil. The excavated soil was included to assess the impact of slope cutting on the stability. Through systematic evaluation of various mesh schemes and nodal configurations, the optimized model was ultimately established, comprising 681,444 nodes and 599,288 finite elements (Fig. 4b). Taking into account the slope lithology and rock mass structure, as well as the actual engineering geological conditions, the model was designed using elasto-plastic material properties and the Mohr–Coulomb constitutive model[4]. The boundary conditions of the model were configured with fixed constraints on all sides, allowing only vertical gravitational forces, while the top surface of the slope remained free from any constraints. To simulate the initial stress field, an elasto-plastic yield criterion was employed, with gravitational loading set at 10 m/s^2. The model's convergence was achieved using the default maximum unbalanced force threshold of 1×10^{-5}, ensuring that the initial ground stress reached equilibrium and the model stabilized under self-weight stress conditions.

The parameters serve as essential data support for numerical simulations, and their accuracy has a direct impact on the reliability of the simulation outcomes. In traditional deterministic approaches, specific values from laboratory tests or field data, such as strength and deformation modulus, are typically used as geo-mechanical

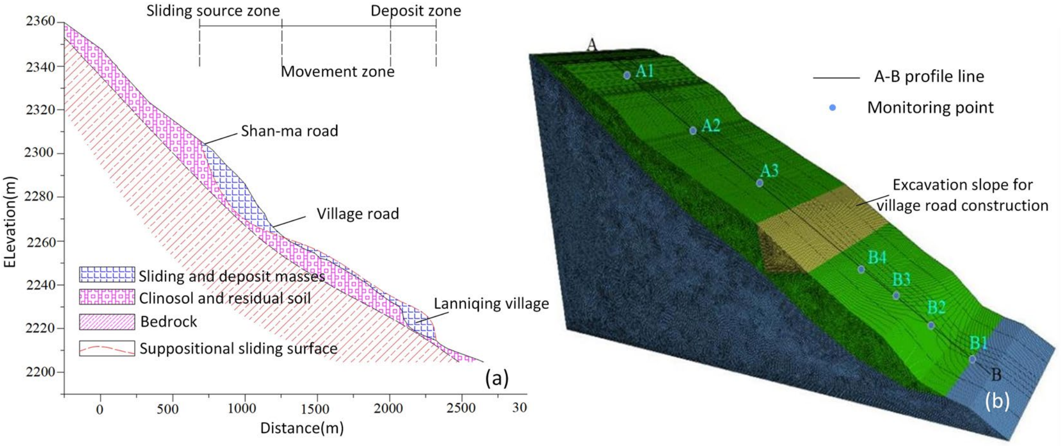

Fig. 4. Cross-section map and computational modeling of Lanniqing landslide. (**a**):The cross-section map was drawn based on field investigations. (**b**):The computational model was constructed using FLAC3D 5.00.

No.	Materials	Density (kg m^{-3})		Elasticity modulus (MPa)	Poisson's ratio (μ)	Bulk modulus (MPa)	Shear modulus (MPa)	c (KPa)		φ (°)	
		(1)	(2)					(1)	(2)	(1)	(2)
1	Mudstone	2000	2300	2622	0.35	2913.33	971.11	1750	1400	40	32
2	Clinosol and residual soil	1850	2000	14	0.2	7.778	5.833	37	29.6	20	16
3	Excavated soil	1850	2000	14	0.2	7.778	5.833	37	29.6	20	16

Table 1. Geotechnical parameters used for numerical simulation of Lanniqing landslide. (1) Natural condition. (2) Rainfall condition.

No.	Analysis conditions	Research contents
1	Gravity loading	Analyze the stress and stability of the slope under natural conditions
2	Gravity loading and slope excavation	Assess slope displacement, shear strain increment, and stability after slope excavation for village road construction
3	Gravity loading and rainfall	Analyze and compare slope displacement, shear strain increment, and stability after rainfall
4	Gravity loading , slope excavation and rainfall	Evaluate and compare slope displacement, shear strain increment, and stability under the combined influence of multiple factors

Table 2. Summary of numerical simulation scenarios for the Lanniqing Slope Under Different Conditions.

input parameters for design or safety evaluations[2,33]. Researchers gathered the physical and mechanical properties of the soil, including soil type, moisture content, and strength, through various methods such as literature reviews. In this study, the mechanical parameters of the sliding-zone soil of the Lanniqing landslide were determined by integrating relevant research findings[8–10,34] and empirical data from local rock and soil masses. The upper layer was characterized using the mechanical properties of colluvial and residual soils, while the bedrock was modeled using the mechanical parameters of mudstone. The specific parameters values are detailed in Table 1.

Calculation conditions and stability analysis

To more effectively evaluate the stability of the Lanniqing slope, this study performed simulations under various conditions, including gravity loading, rainfall, and slope excavation, in order to comprehensively assess the slope's stability and the mechanisms of failure under different factors. The specific calculation conditions and analysis procedures are outlined in Table 2.

This study applies the strength reduction method to calculate the safety factor of the slope under various conditions, such as the natural state, slope cutting, rainfall, and the combined influence of multiple factors. It offers an in-depth analysis of the effects of various external conditions on slope stability. The method focuses on adjusting the strength parameters, cohesion (c) and internal friction angle (φ), by dividing them by the reduction factor (F) and then analyzing the slope stability. The reduction factor F is gradually increased, with calculations repeated until the slope reaches a critical failure state, at which point the resulting reduction factor is identified as the safety factor (Fs)[35]. Currently, slope failure is typically evaluated based on three criteria[4,35]: (1) determining failure through the continuous formation of plastic zones; (2) detecting abrupt changes in displacement at key points; and (3) using calculation non-convergence as an indicator. In this study, the safety

Safety factor *Fs*	Slope stability status
Fs ≥ 1.15	Stable
1.05 ≤ *Fs* < 1.15	Basically stable
1.00 ≤ *Fs* < 1.05	Marginally stable
Fs < 1.00	Unstable

Table 3. Criteria for judging slope stability.

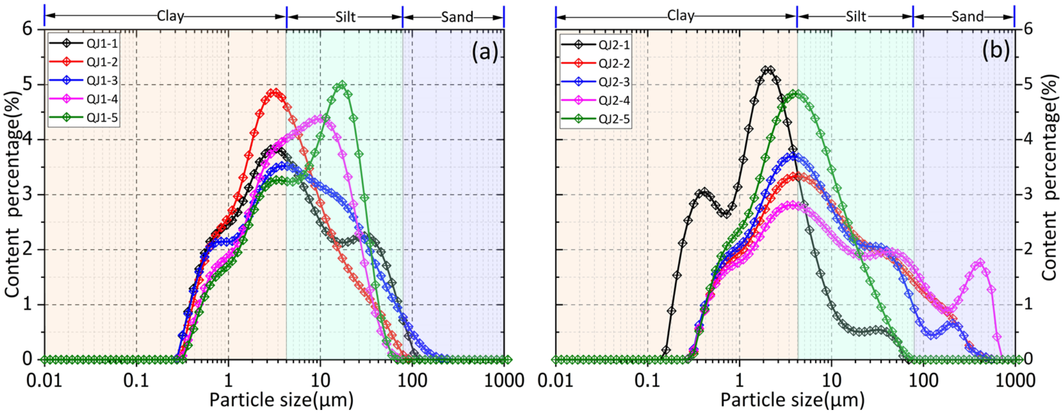

Fig. 5. The particle size distribution curve of soil samples. (**a**): QJ1 sample; (**b**): QJ2 sample.

factor is calculated using the first criterion, while also incorporating the guidelines from the "Chinese Code for Investigation of Landslide Prevention Engineering" (GB/T32864-2016) to perform comprehensive assessment of slope stability (Table 3).

Results and discussion

Laboratory study on soil properties

Particle size composition is a key physical parameter that influences the permeability and mechanical strength of soil samples. The particle size distribution curves are displayed in Fig. 5. Most of the patterns exhibit a single-peak distribution, with a few showing multi-peak characteristics. Based on statistical analysis, the median particle sizes for samples QJ1-1 through QJ1-5 are 4.56, 3.79, 5.64, 5.97, and 7.88 μm, respectively, while for QJ2-1 through QJ2-5, the values are 1.87, 6.93, 5.76, 9.65, and 4.30 μm.

Using the classification method that categorizes particles into clay (less than 0.005 mm), silt (0.005–0.075 mm), and sand (greater than 0.075 mm), it is evident that the soil samples are primarily composed of silt particles, followed by clay particles, while sand particles are relatively minimal. The sample with the highest clay content is QJ2-1, exhibiting clay content of 45.13%, silt content of 49.46%, and sand content of 4.46%. Conversely, the sample with the lowest clay content is QJ1-5, which contains 34.28% clay, 61.65% silt, and 4.13% sand. Overall, all samples have clay content exceeding 30%, with over half of them surpassing 40% clay content. Clay particles are essential to the formation and evolution of landslides. Finer sliding-zone soils indicate greater specific surface area, which facilitates the formation of bound water during rainfall, leading to the higher plasticity index and increased cohesion. The results of liquid limit and plastic limit tests show that liquid limit values range from 36.97 to 49.25%, while plasticity index (IP) values fall between 12.25 and 19.75%, indicating potentially high clay content. This is consistent with the findings from particle size analysis. According to the classification standards for fine-grained soils presented in Fig. 6, most of the soil samples are located near the red line, primarily on the upper side of CL (Clay-Low plasticity), classified as low liquid limit clay. The remaining samples fall into the category of low liquid limit silt. Notably, particles smaller than 0.075 mm make up over 90% of the total composition. These soils, with the high concentration of fine particles, exhibit very low permeability, particularly in the presence of expansive clay. In rainfall conditions, the rate of soil shrinkage can exceed the rate at which pore water pressure dissipates, resulting in increased pore water pressure. This leads to a significant decrease in the soil shear strength, increasing the likelihood of slope failure[36].

Based on the direct test results, the shear stress versus shear displacement curves were plotted, as illustrated in Fig. 7. Under the constant vertical pressure, the shear stress gradually increases with shear displacement, although the rate of increase varies from rapid to slow until the soil samples shear failure. The QJ1 and QJ2 soil samples exhibit similar shear resistance characteristics, however, some curves for the QJ1 samples show a noticeable peak, indicating strain softening behavior. This peak value can be directly interpreted as the shear strength of the soil sample. In contrast, samples without a peak strength demonstrate strain hardening behavior, where the corresponding shear stress at the shear displacement of 4 mm is considered as the shear strength. The characteristics of the curves reveal that at low levels of shear displacement, the shear stress increases quickly,

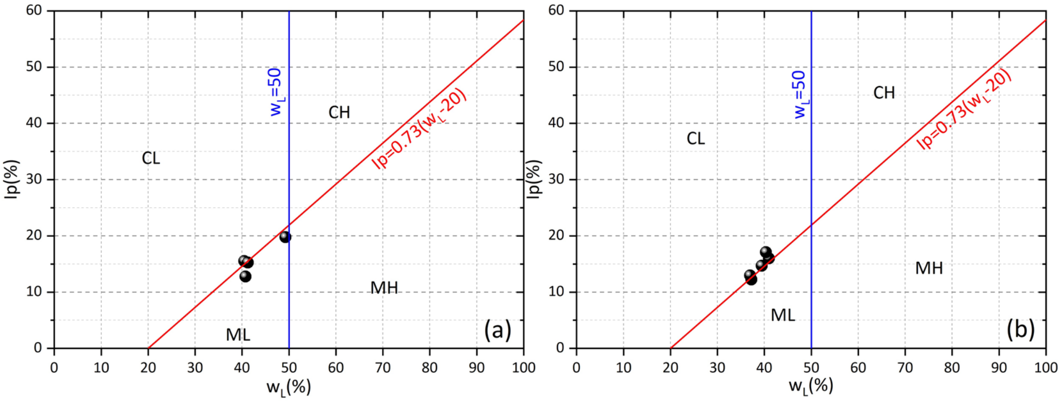

Fig. 6. Classification of soil samples based on the results of liquid limit(w_L), plasticity index(I_p), according to the Unified Soil Classification System (Casagrande,1948)[37]; M, silt; C, clay; H, high plasticity; L, low plasticity. (**a**) QJ1 sample which was missing the data of QJ1-3. (**b**): QJ2 sample.

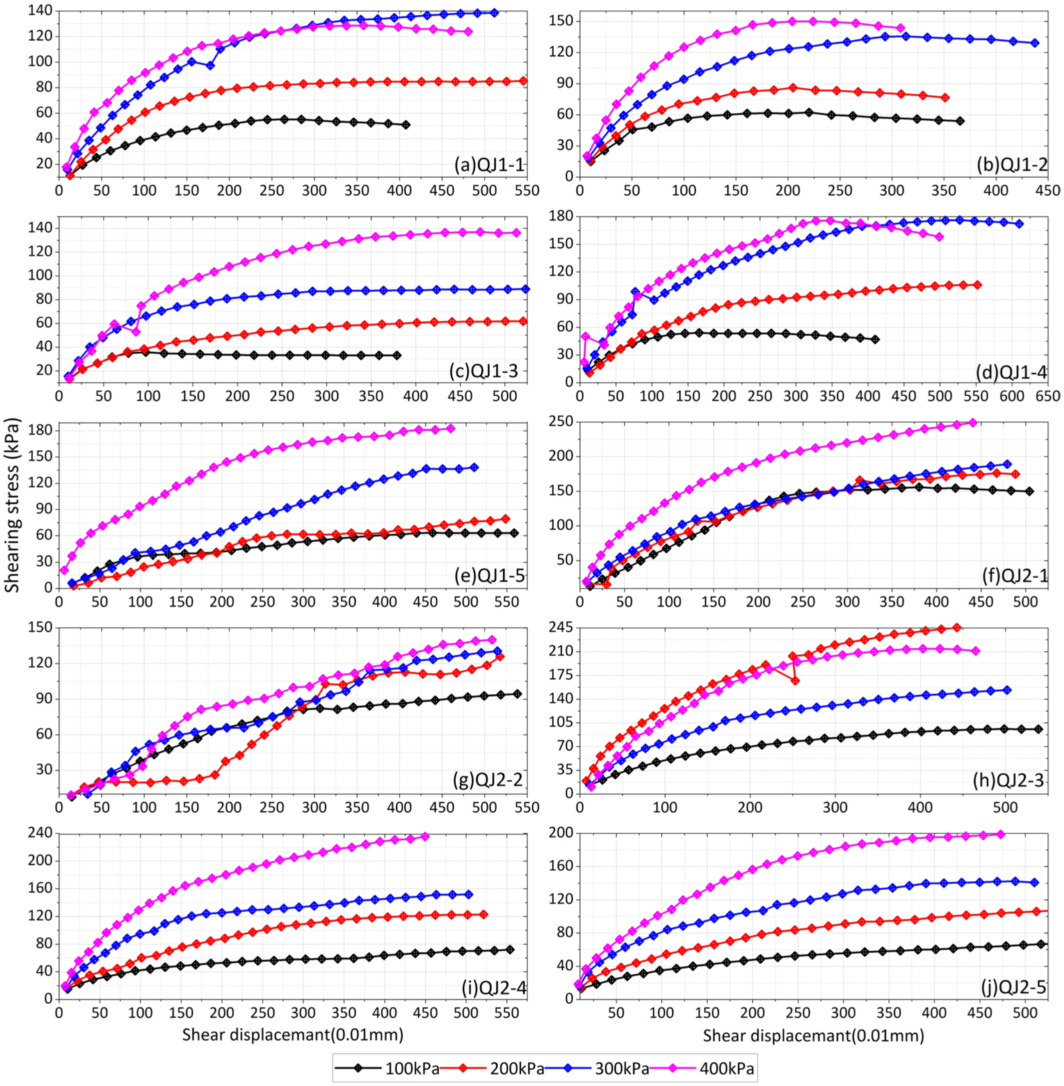

Fig. 7. Relationship between shear displacement and stress of soil samples. For better readability, the x-and y-axis labels are unified.

	Shear strength (kPa)				Cohesive force	Internal friction angle
Sample ID	100 kPa	200 kPa	300 kPa	400 kPa	c (kPa)	φ (°)
QJ1-1	55.09	84.66	134.50	128.80	33.02	15.16
QJ1-2	62.29	86.08	135.53	150.08	30.28	17.22
QJ1-3	35.68	60.50	87.95	99.42	16.02	12.41
QJ1-4	53.99	98.50	168.50	175.75	15.37	23.75
QJ1-5	60.50	64.08	124.80	174.20	5.44	21.89
QJ2-1	155.87	169.13	177.37	242.19	119.34	14.96
QJ2-2	86.21	112.82	116.08	126.21	79.51	6.84
QJ2-3	92.11	145.35	214.41	240.05	44.76	27.02
QJ2-4	63.90	119.04	145.24	228.97	8.93	27.47
QJ2-5	60.22	98.84	139.83	195.39	11.95	24.06

Table 4. The shear strength and its indicators of soil samples.

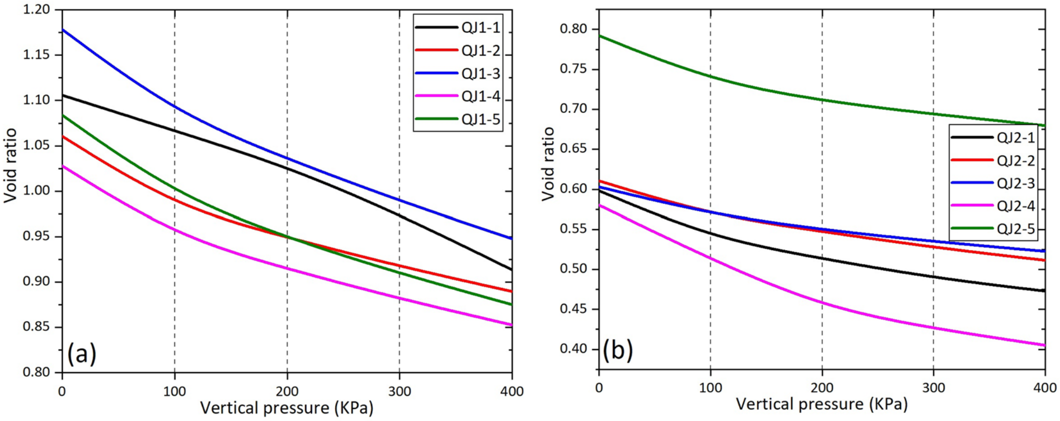

Fig. 8. Relationship between pressure and void ratio of soil samples subjected to vertical pressure deformation process.

then stabilizes as the sample transitions into the creep slip phase, continuing until the shear failure occurs. The correlation between vertical pressure and shear strength enables the determination of shear strength parameters: cohesion (c) and friction angle (φ) (Table 4). Cohesion is derived from the bonding forces and electrostatic attraction between soil particles, which are influenced by clay content and moisture levels. The friction angle results from the roughness of particle surfaces at the shear plane and the interlocking forces created by their interactions, impacted by vertical stress, soil density, particle gradation, and shape. In Fig. 7, some soil samples, such as QJ2-1 and QJ2-2, show largely overlapping curves under different vertical pressures, indicating that the vertical pressure have little impact on the shear strength. In this case, the samples demonstrate high cohesion and low friction angles, except for QJ1-5 and QJ2-4. This is directly related to the high clay content and is consistent with the results of the particle size analysis. Additionally, as shown in Table 4, the shear strength parameters of QJ2-1 are notably higher than those of the other samples. For instance, at a vertical load of 100 kPa, its shear strength reaches 155.87 kPa. This discrepancy is likely due to QJ2-1 being collected from the surface layer, where the moisture content is lower, coupled with its higher clay content, which contributes to increased cohesion and enhanced shear strength. To conclude, the particle size composition significantly affects soil strength and its parameters. Under conditions of increased moisture from rainfall, the high clay content, particularly the presence of chlorite and mica[38], which are layered aluminosilicates and primary sources of clay minerals, further diminishes soil strength, promoting the formation and development of sliding zones, which may ultimately trigger landslides.

The curves depicting the relationship between pressure and void ratio of the soil samples can be derived from the compression tests, as illustrated in Fig. 8. This figure indicates that the initial void ratio of the soil samples is approximately 1.0, with QJ1 displaying void ratio greater than 1.0, which means they are loose, high- compressibility soils. As vertical pressure increases, the void ratio of the soil samples gradually decreases, resulting in downward trend in the curves. The compression curves of QJ1 are steeper than those of QJ2, and the corresponding compression coefficients, as presented in Table 5, range from 0.34 to 0.51 MPa^{-1} for QJ1, which are generally higher than those of QJ2 (0.19–0.31 MPa^{-1}). This suggests that QJ1 exhibits the higher degree of compressibility compared to QJ2. In particular, except for the QJ1-3, which has a compression coefficient of 0.51 MPa^{-1}, exceeding 0.5 MPa^{-1} and classifying it as high compressibility soil, the values of the other soil samples range from 0.1 to 0.5 MPa^{-1}, categorizing them as medium compressibility soils. The void ratio of the

Sample ID	The void ratio of each vertical pressure					Compression coefficient (MPa^{-1})
	Initial	100 kPa	200 kPa	300 kPa	400 kPa	
1–1	1.11	1.07	1.03	0.97	0.91	0.39
1–2	1.06	0.98	0.95	0.92	0.89	0.34
1–3	1.18	1.09	1.04	0.99	0.95	0.51
1–4	1.03	0.95	0.91	0.88	0.85	0.37
1–5	1.08	1.00	0.95	0.91	0.88	0.48
2–1	0.60	0.54	0.51	0.49	0.47	0.26
2–2	0.61	0.57	0.55	0.53	0.51	0.21
2–3	0.60	0.57	0.55	0.53	0.52	0.19
2–4	0.58	0.54	0.51	0.49	0.46	0.31
2–5	0.79	0.74	0.71	0.69	0.68	0.26

Table 5. Results of parameters related to the evaluation of soil sample compressibility.

soil samples does not stabilize even under vertical pressure of 400 kPa, suggesting that there is still potential for further reduction in the void ratio under high pressure. In conclusion, the compression test results indicate that the samples exhibits medium to high compressibility. When considered alongside the shear test results, it is reasonable to infer that the Lanniqing soil samples demonstrate poor mechanical properties.

Numerical simulations results

The numerical simulation results under various calculation conditions are primarily assessed through the horizontal displacement, shear strain increment, and safety factor of the Lanniqing slope. The distribution of the shear strain increment highlights the weaker zones within the slope and facilitates rough estimation of the sliding surface[33]. Initially, the analysis focuses on the Lanniqing slope under natural condition. In terms of horizontal displacement, the maximum displacement is observed near the toe of the slope, where the clinosol and residual soil layers exhibit relatively large displacements. The maximum displacement recorded is 6.24 cm, although the overall displacement remains relatively small (Fig. 9a). At a certain depth, the Lanniqing slope develops shear zone of considerable thickness, leading to changes in the internal stress state and general tendency of downward sliding along the interface between the residual soil layers and bedrock (Fig. 9b). Nevertheless, the safety factor ($Fs = 1.26 \geq 1.15$) indicates that the slope is stable, with no significant deformation, and is still in the concealed phase of landslide. Thus, while there is a tendency for deformation at the edge of the slope under natural condition, but the displacement is minimal, and overall stability is preserved.

Under rainfall conditions, the displacement of the bedrock remains largely consistent with the natural condition. However, the horizontal displacement of the clinosol and residual soil has notably increased compared to the natural condition, with the maximum reaching 17.42 cm at the foot of the slope (Fig. 9c). No significant plastic deformation is detected within the bedrock, while localized zones of shear and tensile failure are present within the accumulation body. The primary shear and tensile failures are concentrated at the interface between the two regions (Fig. 10a). Displacement discontinuities at this boundary further increase the likelihood of irregular deformation and sliding in this area. This results in shear failure at the foot of the slope, where the displacement is maximal. While no significant plastic deformation is noted within the bedrock, the upper soil exhibits localized shear failure zones primarily at their interface. Compared to the natural condition, there is a more pronounced banded zone of strong shear deformation at the interface, extending from the top of the slope and parallel to the slope surface down to the foot. Additionally, the shear strain increment has increased by nearly 21% (Fig. 9d). The impact of rainfall on material strength significantly affects slope stability, with the safety factor of the slope being $Fs = 1.10$, indicating a basic stable condition.

To simulate the excavation scenario for constructing the Lanniqing village road, the soil in the middle-lower parts of the slope was removed. This alteration resulted in significant changes to the horizontal displacement, with deformation primarily concentrated in the upper section of the cutting. The maximum horizontal displacement reached approximately 3.45 m, representing a substantial increase compared to the previous two conditions (Fig. 9e). Due to the absence of timely support during the cutting slope, the upper soil masses experienced unloading deformation under gravity loading, leading to greater potential deformation and shear- tensile failure of the overlying soil, however, significant shear and tensile failure occurs at the rear edge of the cut slope (Fig. 10b). Additionally, the shear strain increment revealed noticeable changes (Fig. 9f), with relatively localized shear deformations occurring on the backside of the cutting. The shear strain values increased significantly, with the maximum located behind the excavated slope toe. Calculations indicated that the safety factor under cutting conditions is $Fs = 0.72$, suggesting an unstable state. Consequently, after the slope was cut, the internal stress state deteriorated sharply, the safety factor decreased significantly, and stability declined rapidly, with deformation concentrated in a localized area behind the cut section, posing the risk of sliding along the deformation surface. Overall, the observed changes in horizontal displacement, shear strain increment, and safety factor clearly demonstrate that the destabilizing effect of slope cutting on stability is significantly pronounced.

The previous analysis concentrated on the effects of single factor on slope stability. However, field studies and analyses reveal that the Lanniqing landslide is likely caused by the combined influences of slope cutting and rainfall. Therefore, the multi-factor coupling analysis is necessary. In the context of multiple factors (Fig. 9g), the horizontal displacement of the slope exhibit significant differences compared to those observed

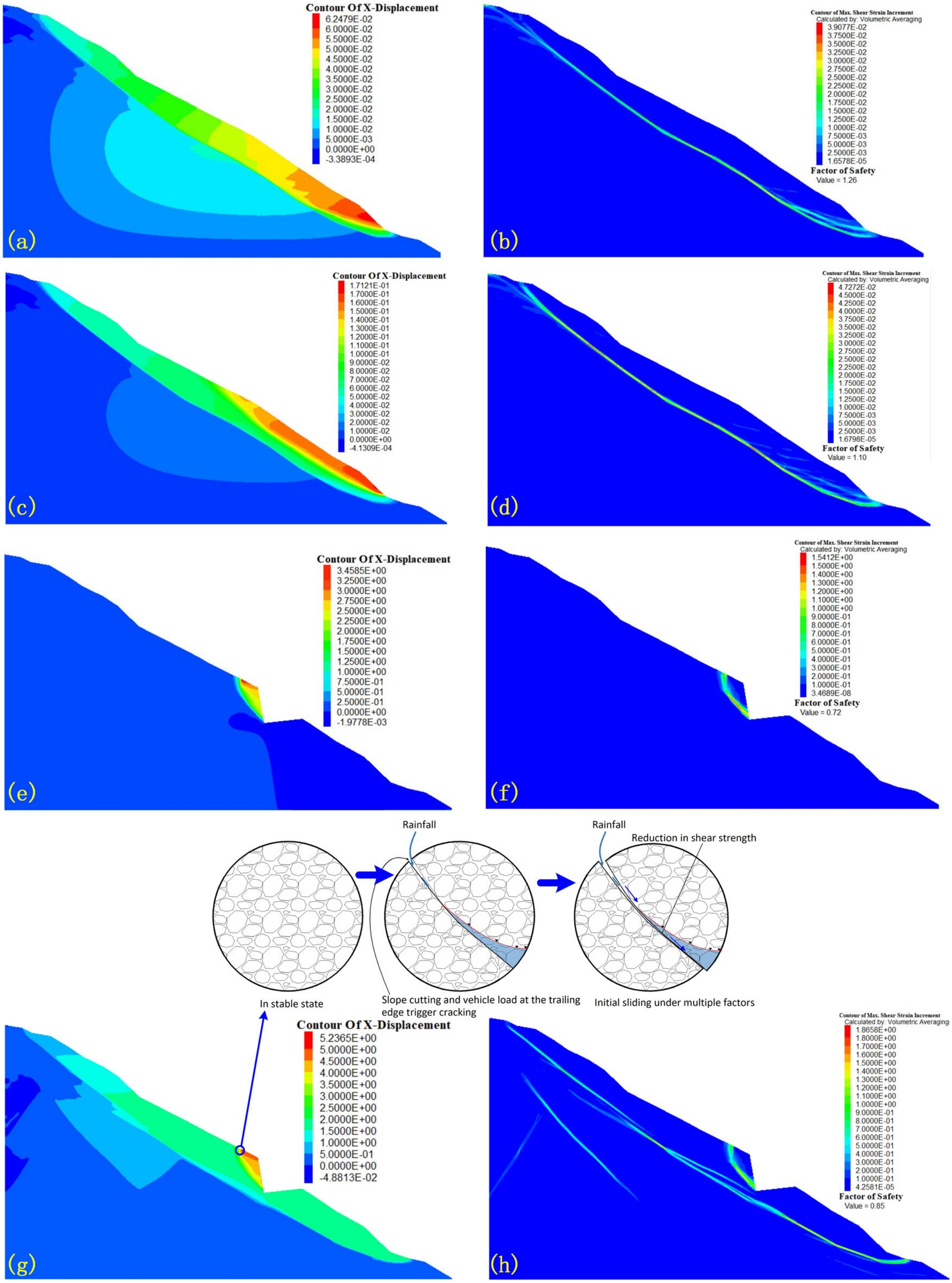

Fig. 9. Horizontal displacement, shear strain increment, and safety factor of the mudpass slope under various conditions: (**a**) and (**b**) show natural state, (**c**) and (**d**) depict rainfall condition, (**e**) and (**f**) represent cut slope condition, and (**g**) and (**h**) illustrate coupling condition.

under isolated conditions of slope cutting or rainfall. When these factors are coupled, the overall horizontal displacement increases notably, particularly at the upper soil following the cutting, where the maximum horizontal displacement reaches approximately 5.23 m, with most clinosol and residual soil materials showing displacements exceeding 3 m. At this stage, distinct tensile failure appears at the rear of the slope, while the shear zone primarily occurs at the interface between the two regions, extending continuously to the slope toe

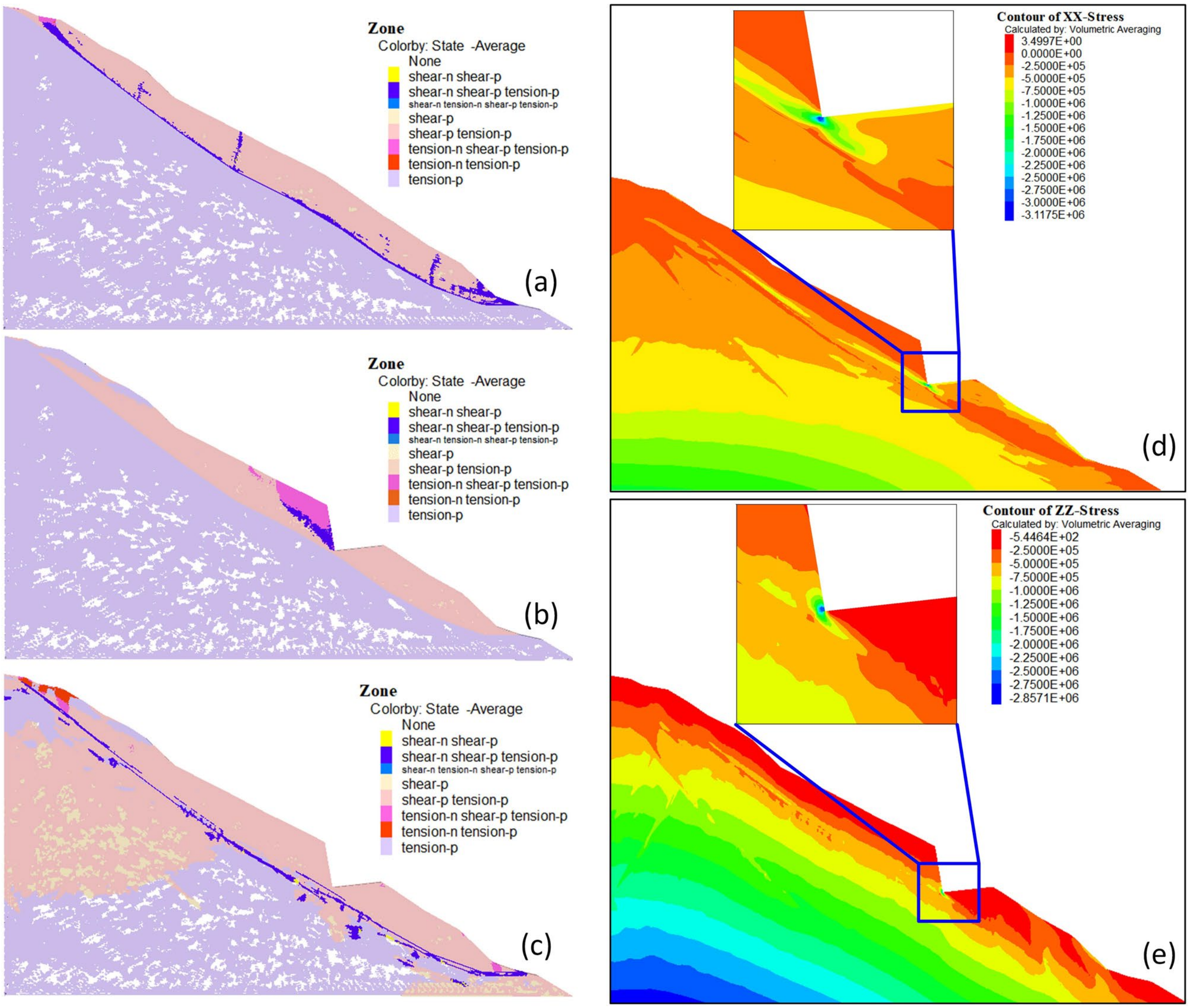

Fig. 10. Distribution of the plastic zone and stress cloud diagrams in horizontal and vertical directions. (**a**–**c**) depict the plastic zone distribution under rainfall condition, cut slope condition, and coupled condition, respectively. (**d**) and (**e**) present the horizontal and vertical stress cloud diagrams under multi-factor coupling condition.

(Fig. 10c). Stress cloud diagrams for the horizontal and vertical directions reveal that, apart from localized range on the slope surface showing horizontal tensile stress, the slope generally remains in a compressive stress state. This is especially evident at the excavated slope toe, where significant stress concentration occurs, with horizontal stress exceeding vertical stress, adversely impacting the stability of the slope within the affected cut area (Fig. 10d,e). This indicates that, under the dual influences of slope cutting and rainfall, the soil loses support, resulting it more prone to downward movement due to gravity loading. Additionally, the impact of rainfall further weakens the soil strength and parameters, leading to a marked increase in the displacement of slope masses. This indicates that slope cutting significantly reduces slope stability, while vehicle loads at the rear edge cause tensile cracks, which enhance rainfall infiltration. Particle size analysis reveals that the sliding zone is rich in clay particles, creating a low-permeability layer that facilitates water accumulation and leading to the formation of the local perched water layer. The resulting increase in pore water pressure and the subsequent reduction in shear strength greatly accelerate the slope failure process (as illustrated in the inset of Fig. 9g). Analysis of shear strain increments reveals two primary potential sliding surfaces under multi-factor coupling (Fig. 9h): one extends from the toe of the slope to the top, aligning with the sliding surface created by slope cutting; the other occurs at the interface between the upper soil and the bedrock, resembling sliding surfaces formed by gravity loading or rainfall, though not identical. Under this multi-factor influence, the slope's safety factor is Fs = 0.85, indicating an unstable state.

In real-world terms, the lanniqing slope is steep, and although deformation trends and potential sliding surfaces may develop under gravity loading and rainfall, the slope generally remains stable. However, ongoing slope cutting for village road construction has significantly compromised its stability. Furthermore, the rear edge of the slope is subjected to continuous traffic loads from the shan-ma road. Coupled with laboratory test results showing high fine particle content, medium to high compressibility, and poor mechanical properties in the slope masses, the heavy rainfall in early September 2019 acted as the triggering factor, ultimately leading to slope instability and resulting in severe casualties and property damage. It should also be noted that the current analysis is based on a two-dimensional simplified model, which may overlook critical three-dimensional effects, and that the laboratory samples used may have limited representativeness due to the inherent heterogeneity of the in-situ slope materials. Despite these limitations, the results still provide valuable insights into the failure mechanisms and offer practical guidance for similar slope stability assessments.

Field investigations, laboratory tests, and numerical simulations reveal that the landslide masses, characterized by specific physical and mechanical properties, form the fundamental basis for landslide occurrences. The slope cutting for village road construction significantly contributes to the deterioration in slope stability, while rainfall serves as the catalyst for Lanniqing landslides. These findings highlight the importance of timely support measures and improved drainage systems, even for small-scale village roads in mountainous areas. Additionally, priority should be given to regular inspections of road embankment deformations, potentially utilizing the low-cost multi-smartphone photogrammetric monitoring system[39], and enhancing remote sensing monitoring. These technical approaches can efficiently and economically achieve real-time monitoring of slope deformations, providing critical data support for landslide early warning and prevention.

Conclusions

This study investigates the Lanniqing landslide in Zhaotong, Yunnan Province, located in southwestern China. By combining field surveys, laboratory experiments, and numerical simulations, it uncovers the physical, shear, and compressive mechanical properties of the sliding-zone soils. Additionally, the research examines slope deformation and stability under both individual and combined factors, aiming to identify the triggers behind the landslide. The key outcomes of the study are summarized as follows:

(1) The liquid limit of soils varies between 36.97 and 49.25%, while the plasticity index ranges from 12.25 to 19.75%. Over 90% of the soil particles are smaller than 0.075 mm, suggesting a high clay content. Most samples consist of low-liquid-limit clays, with some low-liquid-limit silts. These fine-grained soils have low permeability, meaning that under rainfall conditions, pore water pressure dissipates slowly, leading to an increase in pore pressure, which significantly weakens the soil shear strength and makes slope failure more likely.

(2) The majority of soils demonstrate high cohesion and low friction angles, directly associated with their high clay content. The compression coefficients indicate medium–high compressibility. Results from shear and compression tests show that these soils have poor mechanical properties. Under rainfall conditions, as water content increases, the high fine-particle accelerates the development of the sliding zone, promoting further slope instability.

(3) Slope stability analysis indicates that the slope remains stable under natural and rainfall conditions. However, slope excavation for the village road construction has drastically reduced its stability, pushing it into an unstable state, with deformation primarily concentrated on the slope behind the excavated slope toe. Under the combined influence of multiple factors, including increased shear strain, deformation, and continuous traffic loads from the Shan-ma road, progressive instability ultimately leads to slope failure, resulting in severe casualties and property damage.

(4) These findings highlight the critical importance of timely reinforcement measures, improved drainage systems, and continuous monitoring of slope deformation in road construction projects in mountainous regions to mitigate potential instability and prevent disasters.

Data availability

The datasets used and/or analysed during the current study available from the corresponding author on reasonable request. However, access to some data may be restricted due to privacy or copyright concerns.

Received: 3 December 2024; Accepted: 9 September 2025

References

1. Deng, Z. et al. Vegetation-induced modifications in hydrological processes and the consequential dynamic effects of slope stability. *CATENA* **251**, 108793 (2025).
2. Singh, T. N. et al. Evaluating cut slope failure by numerical analysis—A case study. *Nat. Hazards* **47**, 263–279 (2008).
3. Zhu, D. et al. Revival deformation mechanism of Hefeng landslide in the Three Gorges Reservoir based on FLAC3D software. *Procedia Eng.* **15**, 2847–2851 (2011).
4. Chen, Y. & Xu, D. *Fundamentals and Engineering Applications of FLAC/FLAC3D* (China Water & Power Press, 2009).
5. Gao, S. Study and application of surrounding rock control technology for small coal pillar support with steep. [Master's thesis, Shandong University of Science and Technology] (2018).
6. Lirer, S. Landslide stabilizing piles: Experimental evidences and numerical interpretation. *Eng. Geol.* **149–150**, 1–12 (2012).
7. Xiaochao, L. et al. Deformation evolution characteristics and destabilization mechanism of locked slope excavation. *KSCE J. Civ. Eng.* **28**, 2694–2704 (2024).
8. Ma, Y., Su, P. & Li, Y. Three-dimensional nonhomogeneous slope failure analysis by the strength reduction method and the local strength reduction method. *Arab. J. Geosci.* **13**, 2 (2020).
9. Bai, Y. J. et al. Slope structures and formation of rock–soil aggregate landslides in deeply incised valleys. *J. Mt. Sci.* **17**, 59–71 (2020).
10. Xiaojie, Y. et al. Stability and remote real-time monitoring of the slope slide body in the Luoshan mining area. *Int. J. Min. Sci. Technol.* **25**, 761–765 (2015).

11. Cai, W. et al. Prediction of surface deformation induced by mining thin coal seam: A case study of Guanshan coalfield in Sichuan. *Nat. Hazards Res.* **4**, 255–264 (2024).
12. Sun, H., Gao, E. & Zhou, A. Numerical simulation of uneven settlement of municipal solid waste landfill by FLAC3D. *Waste Manag. Res.* **40**, 374–382 (2022).
13. Pan, W., Luo, J., Pan, W. & Zhang, K. The law of instability and failure of the slope of dumping site: A case study in Inner Mongolia, China. *Shock Vib.* **2021**, 6689619 (2021).
14. Huang, R. Q. & Xu, Q. Application of explicit Lagrangian finite-difference method in rock slope engineering. *Chin. J. Rock Mech. Eng.* **14**, 346–354 (1995).
15. Kou, X. D., Zhou, W. Y. & Yang, R. Q. Stability analysis on the high slopes of Three-Gorges Shiplock using FLAC3D. *Chin. J. Rock Mech. Eng.* **20**, 6–10 (2001).
16. Xie, H. P., Zhou, H. W., Wang, J. A., Li, L. Z. & Kwasniewski, M. A. Application of FLAC to predict ground surface displacements due to coal extraction and its comparative analysis. *Chin. J. Rock Mech. Eng.* **18**, 397–401 (1999).
17. Ahmed, Z. et al. Variability effect of strength and geometric parameters on the stability factor of failure surfaces of rock slope by numerical analysis. *Arab. J. Geosci.* **13**, 1112 (2020).
18. Li, C., Liu, G., Guo, L., Zheng, D. & Yuan, X. A new CRITIC-GRA model for stope dimension optimization considering open stoping stability, mining capacity and costs. *Appl. Sci.* **14**, 5249 (2024).
19. Wang, L. et al. Construction of 3D creep model of landslide slip-surface soil and secondary development based on FLAC3D. *Adv. Civ. Eng.* **2020**, 1–15 (2020).
20. Xu, F., Hu, H., Lin, H. & Xie, L. Bedding slope destabilization under rainfall: A case study of Zhuquedong slope in Hunan Province, China. *Appl. Sci.* **14**, 1394 (2024).
21. Delchiaro, M., Seta, M., Martino, S. et al. Tectonic deformation and landscape evolution inducing mass rock creep driven landslides: The Loumar case-study (Zagros Fold and Thrust Belt, Iran). Tectonophysics (2022).
22. Fang, K., Miao, M., Tang, H. et al. Insights into the deformation and failure characteristic of a slope due to excavation through multi-field monitoring: A model test. Acta Geotech. (2022).
23. Chen, M., Yang, X. & Zhou, J. Spatial distribution and failure mechanism of water-induced landslides in the reservoir areas of Southwest China. *J. Rock Mech. Geotech. Eng.* **15**, 442–456 (2023).
24. Chen, M. L., Zhou, J. W. & Yang, X. G. Gravitational failure occurrence and evolution of rock slopes due to dam construction: A case study of three reservoirs in Southwest China. *Rock Mech. Rock Eng.* **57**, 7663–7681 (2024).
25. Wang, J. J. et al. A loess landslide induced by excavation and rainfall. *Landslides* **11**, 141–152 (2014).
26. Robbins, J. et al. Tumbi Landslide, Papua New Guinea: Rainfall induced?. *Landslides* **10**, 673–684 (2013).
27. Ji, J., Zhang, T. & Cui, X. Z. W. Numerical investigation of post-earthquake rainfall-induced slope instability considering strain-softening effect of soils. Soil Dyn. Earthq. Eng. 171 (2023).
28. Zhao, Z. S. & Xu, W. Z. Analysis on the causes and prevention measures of Lufanggou debris flow disaster in Xiaohe Town, Qiaojia County, Yunnan Province. *Value Eng.* **32**, 291–293 (2013).
29. Chen, Y. Y. et al. Study on the characteristics of sliding zone soil and occurrence mechanism of Qiaojia Lanniqing landslide in Zhaotong. *J. Nat. Disasters* **33**, 87–97 (2024).
30. Sichuan Provincial Geological Disaster Command & Sichuan Provincial Department of Natural Resources. Selected Cases of Major Geological Disaster Events and Successful Risk Avoidance: Volume 1. (2021).
31. Zheng, W. et al. 3D geological visualization and numerical modeling of complicated slope. *Chin. J. Rock Mech. Eng.* **26**, 1634–1644 (2007).
32. Liao, Q. et al. Automatic model generation of complex geologic body with FLAC3D based on ANSYS platform. *Chin. J. Rock Mech. Eng.* **24**, 1010–1013 (2005).
33. Gao, D., Mishra, B. & Xue, Y. Numerical simulation of laboratory strength tests using a stochastic approach. *Min. Metall. Explor.* **37**, 4 (2020).
34. Cao, Z., Tang, J., Zhao, X. et al. Failure mechanism of colluvial landslide influenced by the water level change in the Three Gorges Reservoir Area. Geofluids (2021).
35. Sun, S., Lin, H. & Ren, L. Application of FLAC3D in Geotechnical Engineering. Beijing: China Water & Power Press (2011). ISBN: 9787508485447.
36. Wang, F., Zhang, B., Yan, K. et al. Rainfall-induced Guilong landslide-mudflow in a terraced field of southwestern China on 22 June 2022. Landslides 1–14 (2024).
37. Casagrande, A. Classification and identification of soils. *Trans. Am. Soc. Civ. Eng.* **113**, 901–930 (1948).
38. Xu, Z., Ye, H. & Li, L. Particle size characteristics of sliding-zone soil and its role in landslide occurrence: A case study of the Lanniqing landslide in Southwest China. *Front. Earth Sci.* **12**, 1483534 (2024).
39. Fang, K. et al. Development of an easy-assembly and low-cost multismartphone photogrammetric monitoring system for rock slope hazards. *Int. J. Rock Mech. Min. Sci.* **174**, 105655 (2024).

Acknowledgements

This research was financially supported by Yunnan Natural Science Foundation Project (202401AT070119). The authors would also like to acknowledge the support of ANSYS 2019R1 and FLAC3D 5.00 for providing computational tools used in this study.

Author contributions

Xu Zongheng: Conceptualization of the study, methodology design, supervision of the research, and correspondence throughout the submission process. Chen Yunying: Finite element model establishment and analysis, data collection, and drafting of the manuscript. Both authors reviewed, revised, and approved the final version of the manuscript.

Declarations

Competing interests

The authors declare that they have not known competing financial interests or personal relationships that could have appeared to influence the work reported in this paper.

Additional information

Correspondence and requests for materials should be addressed to X.Z.